J. Fluid Mech. (1990), *vol.* 213, *pp.* 149–169
Printed in Great Britain

Flow in the half-filled annulus between horizontal concentric cylinders in relative rotation

By K. S. CHEN,† A. C. KU, T. M. CHAN AND S. Z. YANG
Department of Mechanical Engineering, National Sun Yat-Sen University, Kaohsiung, Taiwan, ROC

(Received 19 October 1988 and in revised form 31 March 1989)

Experimental and theoretical results are presented for the flow in a half-filled annulus between horizontal concentric cylinders with the inner one rotating and the outer one at rest. A laser-Doppler velocimeter was used to measure the mean tangential and/or corresponding turbulent velocity distributions for both the laminar and turbulent regimes. Colour dyes were also used to visualize the flow patterns. The Reynolds number based on the gap width varied from 67 to 3242, which corresponds to a Taylor number ranging from 25 to 1200. From the graph of local moment coefficient versus Taylor number and the visualization results, laminar, transition and turbulent regimes are identified. In the analysis, the governing equations are expressed in stream-function and vorticity forms and expanded in terms of the power series of the annulus aspect ratio. The zero- and first-order solutions are then solved numerically. Various features of the flow, in particular the presence of vortices in the exit end region and their absence from the entry end region, predicted in the analysis, are confirmed by the experimental findings.

1. Introduction

Flow in the annulus of concentric cylinders with either one rotating occurs in many engineering fields and has important applications in bearing lubrication and viscometry. Therefore, work on the topic dates back to 1890, when Couette started investigating the flow in the fully filled annulus between concentric rotating cylinders. In such a case, the entire flow field can readily be solved and is frequently referred to as Couette shear flow; see White (1978), for example. Consequently, subsequent investigations have focused on the stability phenomena, and numerous scientists such as Taylor (1923, 1936), Meksyn (1946), Steinman (1956), Stuart (1958), Davey (1962), Duty and Reid (1964) and Coles (1965) have done experimental, theoretical and numerical studies on the stability and formation of Taylor vortices.

In addition, flow in a partially filled annulus between horizontal concentric cylinders with either one rotating also has important applications. For example, a newly developed electrogalvanizing line in the steel-making industry utilizes a roller-type cell to plate the zinc onto the surface of a steel strip; see Komoda *et al.* (1983) and Nabatame (1984). There, a steel strip wound around a large-diameter conductor roller is soaked in the plating bath. Plating is effected by applying electric currents

† Current address: Institute of Applied Mechanics, National Taiwan University, Taipei, Taiwan, ROC.

between the steel strip (cathode) and an arch-shaped zinc anode placed on an outer, stationary, cylinder. It has been found that the fluid mechanics in the plating cell has a profound influence on the uniformity of the zinc coating on the strip, which strongly depends on the roller speed and annulus gap.

Unfortunately, very few investigations of the flow field in a partially filled annulus between concentric cylinders with the inner one rotating appear to have been reported in the literature. To the authors' knowledge, only Brewster, Grosberg & Nissan (1959) have done an investigation in an almost, but not entirely, filled annulus. However, their analysis and experiments were mainly focused on the stability problem in the parallel core flow far from the free surfaces. Moreover, flow fields near the two free surfaces were not considered.

It is the purpose of this study to investigate experimentally and theoretically the flow in a half-filled annulus with the inner one rotating and the outer one at rest. The experimental results are obtained with the aid of a laser-Doppler velocimeter (LDV) and colour-dye visualization. Asymptotic expansions in conjunction with the finite-difference method are employed to solve the flow field in the laminar regime. From these, the streamlines and velocity distributions are obtained and compared with the experimental results. The upper limit of the annulus aspect ratio for which asymptotic solutions are valid is also discussed.

Some of the results presented in this paper have been reported briefly at the Third International Symposium on Transport Phenomena in Thermal Control (see Chen & Chan 1988; Chen, Yang & Humphrey 1988).

2. Experimental study

2.1. *Apparatus and procedure*

The test section had three parts: an inner cylinder, an outer cylinder and rectangular container, as shown in figure 1. The rectangular container was made of Plexiglas with length 345 mm, width 255 mm, height 271 mm, and thickness 12.5 mm. The inner cylinder was made of reinforced plastic with radius $R_i = 65.5$ mm, and axial length 300 mm. A copper rod of radius 12 mm served as the rotating axis of the inner cylinder and was mounted on the two sides of the rectangular container by ball-type bearings. The outer cylinder was also made of transparent Plexiglas with radius $R_o = 74.5$ mm and was mounted onto the container by six screws. The container was filled with water of kinematic viscosity $\nu = 0.9 \times 10^{-6}$ m^2/s, to the level of the centre of the inner cylinder. To prevent some of the water and droplets being carried away by the rotating cylinder, wax was coated on the surface of the inner roller. This was done by immersing the inner cylinder in a bath of melting wax and then pulling it out slowly along its axis. The thickness of the wax was about 0.5 mm.

A pair of pulleys, one mounted on one end of the rotating axis and one mounted on the shaft of a d.c. motor, were connected by string. The rotation speed of the inner cylinder could be varied by adjusting the motor speed or by changing the sizes of the pulleys. The revolution speed, n, of the inner cylinder in the experiment was in the range of 1 to 45 r.p.m., which corresponded to a rotation speed, $\Omega (= (2\pi/60) \times n)$, in the range of 0.105 to 4.712 rad./s. The Reynolds number $Re (= R_o - R_i)\,\Omega R_i/\nu)$, ranged from 67 to 3242 at an annulus aspect ratio A $(= (R_o - R_i)/R_i) = 0.137$. The Taylor number $Ta (= Re A^{\frac{1}{2}})$ ranged from 25 to 1200. To avoid the vibration of the test section induced by the d.c. motor, supporting tables for the test section and d.c. motor were completely separated.

The optical components of the laser-Doppler velocimeter consist of one Spectra-

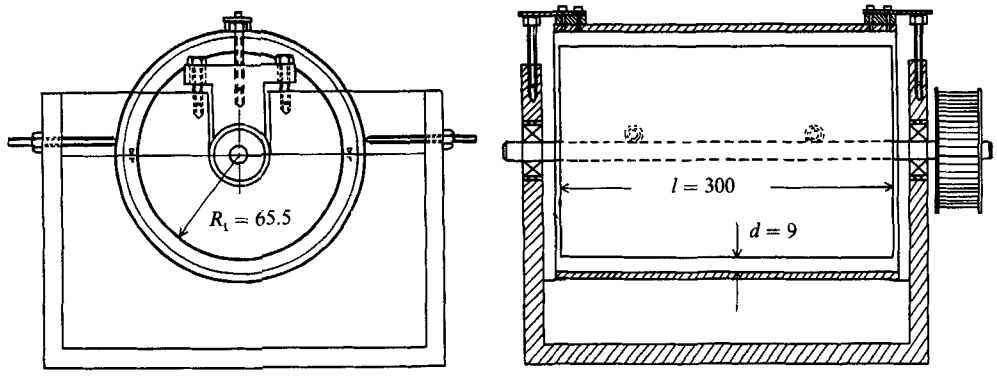

FIGURE 1. Schematic of test section (dimensions in mm).

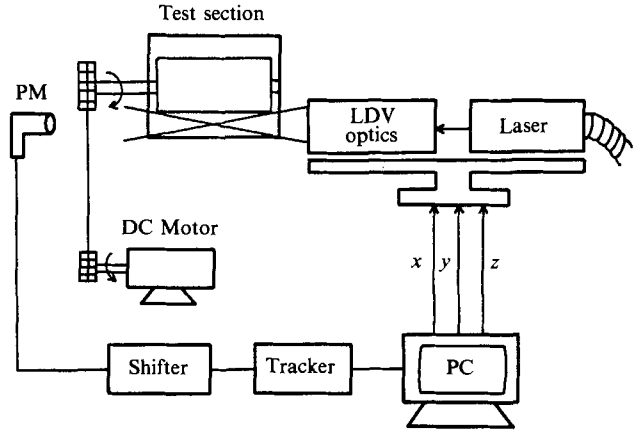

FIGURE 2. Sketch of the optical system and test apparatus.

physics 3W Argon laser, one-component Dantec 55X series optics (including a 40 MHz Bragg cell), and an RCA photomultiplier (PM). The signal processors are a Dantec 55N11 electronic frequency shifter, a Dantec 55N21 frequency tracker and a 16-bit IBM-compatible personal computer for data acquisition, storage and reduction. The laser and the optical components are placed on an optical table, which is equipped with x-, y- and z-traversing mechanisms. The movement of the table in each direction is controlled by a reduced a.c. motor. The traversing distance in each direction is measured by a Mitutoyo optical scale with a digital readout in ± 0.005 mm increments. The forward scattering mode was employed. This was done by placing the PM on the other side of the test section, with an arm connecting the supporting table of the PM to the optical table. Movement of the PM detector is therefore in phase with the optical table. Mean and turbulent velocities were determined from the formulae

$$\bar{V}_\theta = \frac{\sum V_{\theta,i}}{N}, \tag{1}$$

$$\bar{v}_\theta = \left[\frac{\sum (V_{\theta,i} - \bar{V}_\theta)^2}{N}\right]^{\frac{1}{2}} \tag{2}$$

where N is the number of instantaneous realizations. In this study $N = 500$ was used. For the measurements, the focal point of the laser beams was adjusted to the middle of the test section in the axial direction. The focal length for the object was 310 mm, and 150 mm for the detector. A sketch of the optical system and the test apparatus is shown in figure 2.

Red or blue ink was introduced by an injector into the flow for visualization. The needle of the injector was placed in the flow through holes drilled on the upper surface of the outer cylinder. The injector was equipped with a screw for micro-adjusting the amount of ink, and was attached to the container with a supporting arm. Snapshots were taken from the front of the test section with an exposure time of 0.001 s in most cases. Uniformity of the flow in the axial direction was also checked by the colour-dye visualizations and velocity measurements. Results confirm that the flow is essentially two-dimensional with no axial variations except for end effects.

2.2. *Results*

All results were obtained when the inner cylinder was rotating at a constant angular speed in a counter-clockwise direction. For ease of discussion the flow region near the free surface where the inner cylinder moves into the fluid is referred to as the 'entry region'; the 'exit region' is that where the inner cylinder moves out of the fluid; and the 'core region' is that in the bottom middle portion of the annulus.

2.2.1. *Laminar regime*

The flow patterns at the entry, core and exit regions respectively for $Ta = 80$ and $A = 0.137$ are shown in figure 3(a–c) (Plate 1). These pictures were taken with a 40 cm focal length. It is seen from figure 3(a–c) that the rotation of the inner cylinder causes the fluid layer adjacent to it to move, owing to the viscous shear, towards the free surface at the exit end and then make a 180° turn and flow back into the core region. As the outer fluid layer flows towards the free surface at the entry end, it makes another 180° turn and thus forms a two-dimensional recirculation region, in a direction opposite to that of the roller. The flow makes a smooth 180° turn at the entry end but a vortex cell and 'necking' below the free surface occur in the exit end. A close-up photo taken with a 20 cm focal length shows (see figure 3d, Plate 1) that there is an even smaller cell right below the necking place. It is seen from figure 3(c) that the streamlines are essentially parallel in the core region.

The tangential velocity profiles $\bar{V}_\theta$ at various θ-sections are depicted in figure 4. Notice that θ is measured counterclockwise with the origin at the centre of the inner cylinder; and $\theta = 0°$ and 180° correspond to the sections at the entry and exit free surfaces, respectively. In the plots, coordinates have been normalized according to

$$\hat{V}_\theta = \hat{V}_\theta/(R_i\Omega), \quad \hat{r} = (r-R_i)/(R_o-R_i), \tag{3a, b}$$

where r is the radial distance measured from the origin.

It is seen from figure 4 that there is a zero-crossing point, $\hat{r}_c$, in each θ-section. The inner fluid layer ($\hat{r} < \hat{r}_c$) moves from the entry end to the exit end; and the outer fluid layer ($\hat{r} > \hat{r}_c$) moves in the reverse direction. The zero-crossing point, $\hat{r}_c$, increases as θ increases. However, $\hat{r}_c$ remains almost unchanged, with a value of $\frac{1}{3}$, in the bottom core zone (i.e. $60° < \theta < 120°$). The maximum speed of the reversed fluid layer and its radial location decrease as fluid moves from the exit end to the entry end. For example, $\hat{V}_{max} = 0.55$ ($\hat{r} = 0.8$), 0.33 ($\hat{r} = 0.66$), 0.12 ($\hat{r} = 0.39$) at $\theta = 170°$, 90° and 10°, respectively. Note that the small vortex cell is located in the section where $\theta = 150° \sim 170°$; and $\hat{V}_{max} = \frac{1}{3}$ at $\hat{r} = \frac{2}{3}$ in the bottom core zone.

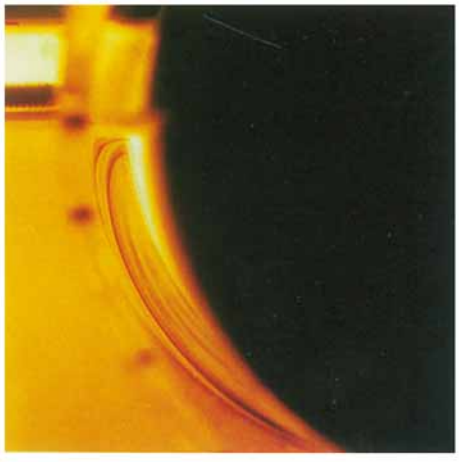

(a)

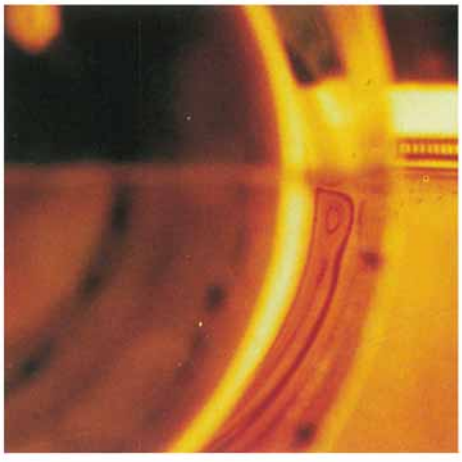

(c)

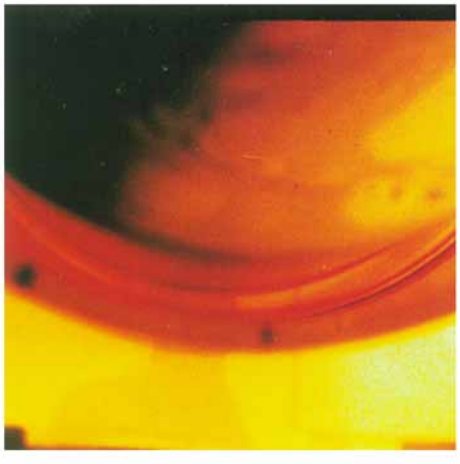

(b)

(d)

FIGURE 3. Flow pattern at Ta=80 and A=0.137: *(a)* for entry region, (b) for core region, (c) for exit region, (d) close-up view at exit end.

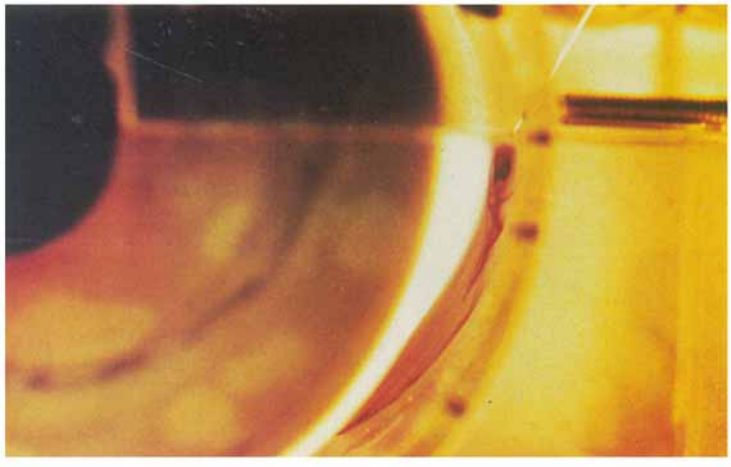

(a)

(b)

FIGURE 7. Flow pattern at Ta=117 and A=0.137: *(a)* front view, *(b)* side view.

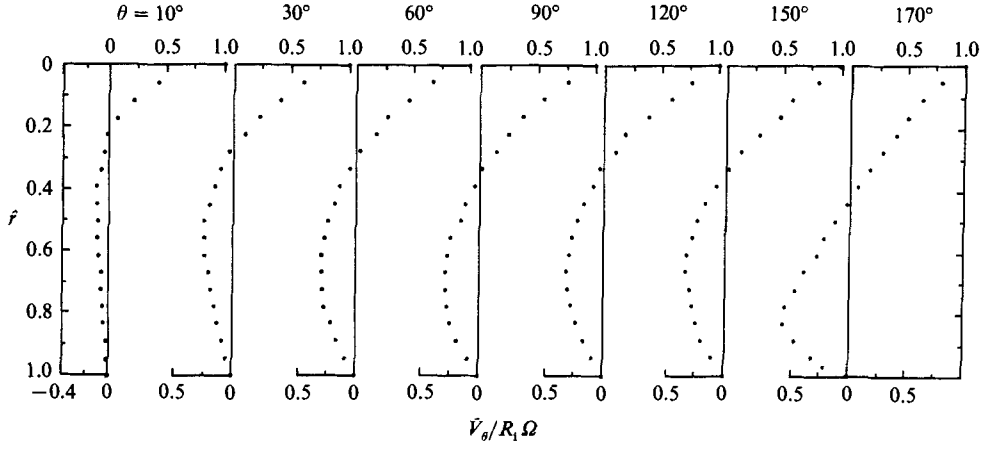

FIGURE 4. Mean tangential velocity profiles at various θ-sections at $Ta = 80$ and $A = 0.137$.

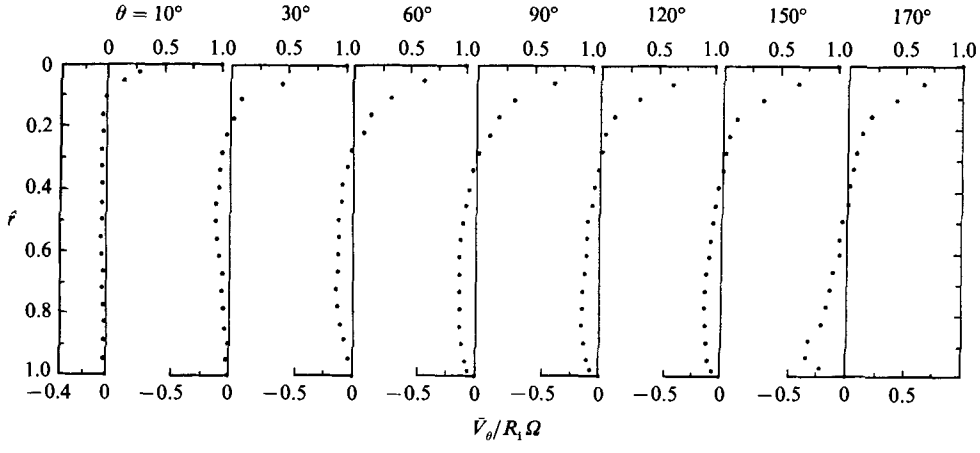

FIGURE 5. Mean tangential velocity profiles at various θ-sections at $Ta = 524$ and $A = 0.137$.

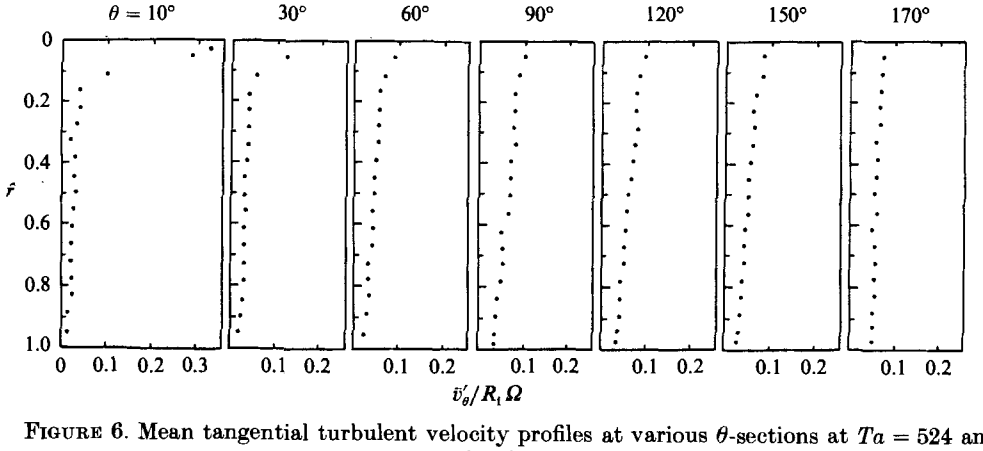

FIGURE 6. Mean tangential turbulent velocity profiles at various θ-sections at $Ta = 524$ and $A = 0.137$.

Radial section (θ) (deg.)	10	30	60	90	120	150	170
zero-crossing point ($\hat{r}$)	0.12	0.19	0.28	0.29	0.32	0.32	0.42
Max. reversed velocity ($\hat{V}_\theta$)	0.04	0.12	0.14	0.15	0.15	0.15	0.27
Position of max. reversed velocity ($\hat{r}$)	0.33	0.50	0.55	0.69	0.78	0.79	0.92

TABLE 1. Some variables for the mean velocity profiles shown in figure 5 for $Ta = 524$ and $A = 0.137$

2.2.2. *Turbulent regime*

The profiles of mean tangential and turbulent velocities at various θ-sections are shown in figures 5 and 6. Table 1 lists the zero-crossing point, the maximum reversed velocity and its radial distance for $Ta = 524$ and $A = 0.137$ at various cross-sections. It can be seen that variations of these quantities are larger in the entry and exit zones but smaller in the core zone. However, compared with those in the laminar regime, the zero-crossing points move closer to the inner cylinder; values of the maximum reversed velocity and its radial distance at each section decrease: that is, the inner fluid layer is thinner in the turbulent regime than in the laminar regime.

Figure 6 shows that at each θ-section turbulent velocity is largest near the inner cylinder and smallest near the outer cylinder. This is particularly noticeable near the entry region (e.g. at $\theta = 10°, 30°$). This may be due to the disturbance resulting from the motion of the inner cylinder in the fluid. However, the profiles of turbulent velocity distributions are quite similar at sections where $\theta \geqslant 60°$, and more uniformly distributed compared with those in the entry sections.

2.2.3. *Identification of the flow regimes*

The flow patterns at a higher Taylor number, $Ta = 117$, are shown in figure 7 (a, b) (Plate 2), which shows that there is some irregular mixing in the flow, and streamlines are not so clearly distinguished as those shown in figure 3 (a–c) for $Ta = 80$. This suggests that flow field at $Ta = 117$ is not in the laminar regime.

Apart from using flow visualization, attempts were also made to measure the local coefficient of moment at various Ta to identify the flow regimes. This is done by measuring the mean tangential velocity using LDV at a fixed point 0.3 mm away from the inner cylinder at a radial section $\theta = 135°$, for various Ta. The local moment coefficient, $C_{M,\theta}$, can be derived according to

$$C_{M,\theta} = \frac{M_\theta}{\frac{1}{2}\rho R_1^4 \Omega_l^2} \approx \frac{\mu\left[r\frac{\partial}{\partial r}\left(\frac{\bar{V}_\theta}{r}\right)\right]_{r=R_1} R_1^2 l}{\frac{1}{2}\rho R_1^4 \Omega^2 l} \approx \frac{\nu\left(\frac{\Delta \bar{V}_\theta}{\Delta r}\right)}{\frac{1}{2}R_1^2 \Omega^2}. \tag{4}$$

Notice that in evaluating the shear stress at the wall ($r = R_1$), the term ($\bar{V}_\theta/r$) has been neglected since $\Delta r/R_1 = 0.3/65.5 \ll 1$.

The plot of $C_{M,\theta}$ versus Ta at $\theta = 135°$ is shown in figure 8, from which, together with the visualization results, the following flow regimes (labelled 1–4) can be identified:

$$\left.\begin{array}{l} Ta < 92: \text{laminar} \\ 92 < Ta < 150: \text{unstable laminar} \\ 150 < Ta < 500: \text{turbulent growth} \end{array}\right\} \text{transition}$$
$$Ta > 500: \text{fully turbulent}$$

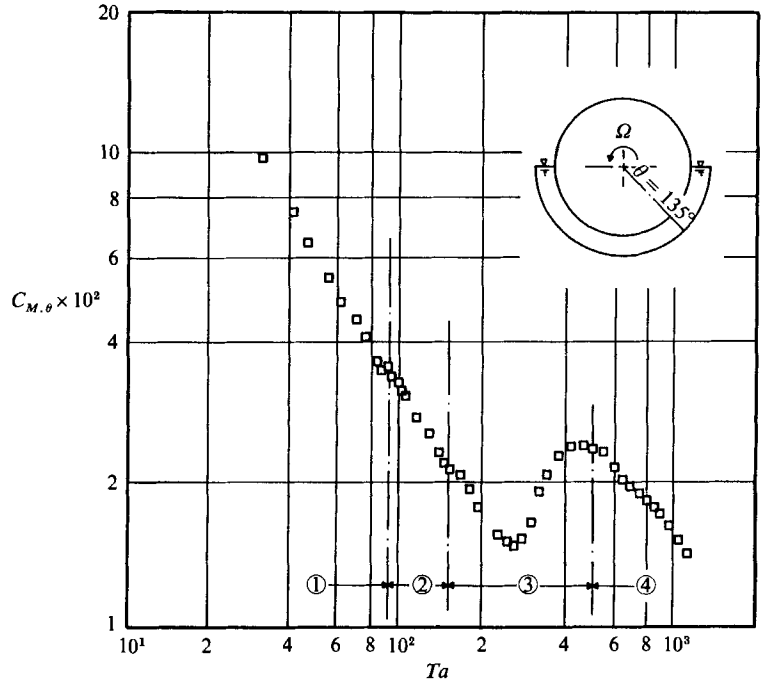

FIGURE 8. Local moment coefficient versus Ta at section $\theta = 135°$.

The result obtained by Brewster *et al.* (1959) in an almost, but not entirely, filled annulus shows that the unstable laminar regime occurs at $Ta = 104$. The present result shows that transition starts at a smaller value, $Ta = 92$. This is because, as the height of free surface above the bottom core decreases, transition starts earlier since the vortex cell in the exit end increases its influence on the core flow.

3. Theoretical study

3.1. *Governing equations*

The governing equations for steady, two-dimensional, incompressible, laminar flow written in stream-function and vorticity forms are

$$\nabla \cdot (V\omega) - \nu \nabla^2 \omega = 0, \tag{5}$$

$$\nabla^2 \psi + \omega = 0. \tag{6}$$

In the above, V, ω, and ψ are respectively, the velocity, vorticity and stream function; and ν is the kinematic viscosity of the fluid. Substituting (6) into (5) and expanding it in cylindrical coordinates yields a single stream function:

$$\frac{\partial \psi}{\partial \theta}\left(r^3 \frac{\partial^3 \psi}{\partial r^3} + r^2 \frac{\partial^2 \psi}{\partial r^2} - r \frac{\partial \psi}{\partial r} + r \frac{\partial^3 \psi}{\partial \theta^2 \partial r} - 2 \frac{\partial^2 \psi}{\partial \theta^2}\right) - \frac{\partial \psi}{\partial r}\left(r^2 \frac{\partial^3 \psi}{\partial r^2 \partial \theta} + r^2 \frac{\partial^2 \psi}{\partial r \partial \theta} + r \frac{\partial^3 \psi}{\partial \theta^3}\right)$$
$$= \nu\left(r^4 \frac{\partial^4 \psi}{\partial r^4} + 2r^3 \frac{\partial^3 \psi}{\partial r^3} - r^2 \frac{\partial^2 \psi}{\partial r^2} + r \frac{\partial \psi}{\partial r} + 4 \frac{\partial^2 \psi}{\partial \theta^2} - 2r \frac{\partial^2 \psi}{\partial \theta^2 \partial r} + 2r^2 \frac{\partial^4 \psi}{\partial \theta^2 \partial r^2} + \frac{\partial^4 \psi}{\partial \theta^4}\right). \tag{7}$$

The boundary conditions are

(i) for $r = R_i$: $$V_r = \frac{\partial \psi}{\partial \theta} = 0, \quad V_\theta = \frac{\partial \psi}{\partial r} = \Omega R_i = U_i; \tag{8, 9}$$

(ii) for $r = R_o$: $$V_r = \frac{\partial \psi}{\partial \theta} = 0, \quad V_\theta = \frac{\partial \psi}{\partial r} = 0; \tag{10, 11}$$

(iii) for $\theta = 0, \pi$: $$V_\theta = \frac{\partial \psi}{\partial r} = 0, \quad \frac{\partial V_r}{\partial \theta} = \frac{\partial^2 \psi}{\partial \theta^2} = 0. \tag{12, 13}$$

That is, the flow satisfies the no-slip condition on the solid walls and zero-shear stress condition on the free surfaces. In the above, V_r and V_θ are the velocity components in the radial and tangential directions, respectively. In the present work, free surfaces are assumed flat, and results are justified by comparing with the measurements (see §4).

The following dimensionless parameters are used:

$$\left.\begin{aligned} A = \frac{R_o - R_i}{R_i}, \quad \hat{r} = \frac{r - R_i}{R_o - R_i}, \quad \hat{V}_r = \frac{V_r}{\Omega R_i}, \\ \hat{V}_\theta = \frac{V_\theta}{\Omega R_i}, \quad \psi^* = \frac{\psi}{(\Omega R_i)(R_o - R_i)}. \end{aligned}\right\} \tag{14}$$

Substituting (14) into (7) yields the dimensionless form

$$\begin{aligned} \frac{\partial \psi^*}{\partial \theta}\Big[& A(A\hat{r}+1)^3 \frac{\partial^3 \psi^*}{\partial \hat{r}^3} + A^2(A\hat{r}+1)^2 \frac{\partial^2 \psi^*}{\partial \hat{r}^2} - A^3(A\hat{r}+1)\frac{\partial \psi^*}{\partial \hat{r}} \\ & + A^3(A\hat{r}+1)\frac{\partial^3 \psi^*}{\partial \theta^2 \partial \hat{r}} - 2A^4 \frac{\partial^2 \psi^*}{\partial \theta^2}\Big] - \frac{\partial \psi^*}{\partial \hat{r}}\Big[A(A\hat{r}+1)^3 \frac{\partial^3 \psi^*}{\partial \hat{r}^2 \partial \theta} \\ & + A^2(A\hat{r}+1)^2 \frac{\partial^2 \psi^*}{\partial \hat{r} \partial \theta} + A^3(A\hat{r}+1)\frac{\partial^3 \psi^*}{\partial \theta^3}\Big] \\ = \frac{1}{Re}\Big[& (A\hat{r}+1)^4 \frac{\partial^4 \psi^*}{\partial \hat{r}^4} + 2A(A\hat{r}+1)^3 \frac{\partial^3 \psi^*}{\partial \hat{r}^3} - A^2(A\hat{r}+1)^2 \frac{\partial^2 \psi^*}{\partial \hat{r}^2} \\ & + A^3(A\hat{r}+1)\frac{\partial \psi^*}{\partial \hat{r}} + 4A^4 \frac{\partial^2 \psi^*}{\partial \theta^2} - 2A^3(A\hat{r}+1)\frac{\partial^3 \psi^*}{\partial \theta^2 \partial \hat{r}} \\ & + 2A^2(A\hat{r}+1)^2 \frac{\partial^4 \psi^*}{\partial \theta^2 \partial \hat{r}^2} + A^4 \frac{\partial^4 \psi^*}{\partial \theta^4}\Big]. \end{aligned} \tag{15}$$

Non-dimensionalizing the boundary conditions (8)–(13) yields

(i) for $\hat{r} = 0$: $$\psi^* = 0, \quad \frac{\partial \psi^*}{\partial \hat{r}} = -1; \tag{16}$$

(ii) for $\hat{r} = 1$: $$\psi^* = \frac{\partial \psi^*}{\partial \hat{r}} = 0; \tag{17}$$

(iii) for $\theta = 0, \pi$: $$\psi^* = \frac{\partial^2 \psi^*}{\partial \theta^2} = 0. \tag{18}$$

Inspection of (15)–(18) reveals that there are two dimensionless parameters, which are Re and A, or Ta $(= ReA^{\frac{1}{2}})$ and A.

In the case where $R_1 \gg d$ $(d = R_0 - R_i)$, or $A \ll 1$, the flow structure can be divided into two parts: (a) the core flow region, in which the lengthscale of the flow is R_1 and streamlines are parallel; (b) the two-end zones, in which the lengthscale of the flow is d and the flow makes 180° turns along the free surfaces. In what follows regular perturbation will be employed to solve the two flow regimes. The continuity condition serves as the requirement for matching the core flow with the end zone flows.

3.2. *The core flow region*

Since the streamlines in the core region, far away from the two turning ends, are parallel as $A \to 0$, we seek a core solution that is independent of θ. That is

$$\frac{\partial^n \psi^*}{\partial \theta^n} = 0; \quad n = 1, 2, 3, \ldots. \tag{19}$$

Hence, the governing equation (15) can be reduced to

$$(A\hat{r}+1)^3 \frac{\partial^4 \psi^*}{\partial \hat{r}^4} + 2A(A\hat{r}+1)^2 \frac{\partial^3 \psi^*}{\partial \hat{r}^3} - A^2(A\hat{r}+1)\frac{\partial^2 \psi^*}{\partial \hat{r}^2} + A^3 \frac{\partial \psi^*}{\partial \hat{r}} = 0. \tag{20}$$

Equation (20) shows that the core flow is independent of Re. We seek the asymptotic solution for the core flow, by a regular expansion in terms of A. That is, for $A \ll 1$,

$$\psi^*_{\text{core}} = \psi^*_c = \psi_0 + A\psi_1 + A^2\psi_2 + \ldots. \tag{21}$$

Substituting (21) into (20) and equating terms of like order in A yields a sequence of linear differential equations for the unknown functions ψ_i as follows:

(i) $O(A^0)$:
$$\frac{\mathrm{d}^4 \psi_0}{\mathrm{d}\hat{r}^4} = 0; \tag{22}$$

(ii) $O(A^1)$:
$$3\hat{r}\frac{\mathrm{d}^4 \psi_0}{\mathrm{d}\hat{r}^4} + \frac{\mathrm{d}^4 \psi_1}{\mathrm{d}\hat{r}^4} + 2\frac{\mathrm{d}^3 \psi_0}{\mathrm{d}\hat{r}^3} = 0, \tag{23}$$

(iii) $O(A^2)$:
$$3\hat{r}^2\frac{\mathrm{d}^4 \psi_0}{\mathrm{d}\hat{r}^4} + 3\hat{r}\frac{\mathrm{d}^4 \psi_1}{\mathrm{d}\hat{r}^4} + \frac{\mathrm{d}^4 \psi_2}{\mathrm{d}\hat{r}^4} + 4\hat{r}\frac{\mathrm{d}^3 \psi_0}{\mathrm{d}\hat{r}^3} + 2\frac{\mathrm{d}^3 \psi_1}{\mathrm{d}\hat{r}^3} - \frac{\mathrm{d}^2 \psi_0}{\mathrm{d}\hat{r}^3} = 0. \tag{24}$$

Similarly, rearrange the boundary conditions of like order in A to yield

$$\text{for } \begin{cases} \hat{r} = 0 \\ \hat{r} = 1: \end{cases} \quad \psi_0 = 0, \quad \frac{\mathrm{d}\psi_0}{\mathrm{d}\hat{r}} = -1, \quad \psi_0 = \frac{d\psi_0}{\mathrm{d}\hat{r}} = 0; \tag{25}$$

$$\text{for } \hat{r} = 0, 1: \quad \psi_i = \frac{\mathrm{d}\psi_i}{\mathrm{d}\hat{r}} = 0 \quad (i = 1, 2, 3, \ldots). \tag{26}$$

Because (22)–(24) are ordinary differential equations, they can be solved by direct integration with boundary conditions given in (25) and (26). The results are

$$\psi_0 = -\hat{r}^3 + 2\hat{r}^2 - \hat{r}, \tag{27}$$

$$\psi_1 = \tfrac{1}{2}\hat{r}^4 - \hat{r}^3 + \tfrac{1}{2}\hat{r}^2, \tag{28}$$

$$\psi_2 = -\tfrac{7}{20}\hat{r}^5 + \tfrac{2}{3}\hat{r}^4 - \tfrac{17}{60}\hat{r}^3 - \tfrac{1}{30}\hat{r}^2. \tag{29}$$

The corresponding velocity $\hat{V}_i$, for $i = 0, 1, 2, \ldots$, for each order can be obtained from (14) as follows:

$$\hat{V}_0 = 3\hat{r}^2 - 4\hat{r} + 1, \tag{30}$$

$$\hat{V}_1 = -2\hat{r}^2 + 3\hat{r}^2 - \hat{r}, \tag{31}$$

$$\hat{V}_2 = \tfrac{7}{4}\hat{r}^4 - \tfrac{8}{3}\hat{r}^3 + \tfrac{17}{20}\hat{r}^2 + \tfrac{1}{15}\hat{r}. \tag{32}$$

Notice that in the case of $d \sim o(R_i)$, the core solution is dependent both on θ and $\hat{r}$, and is not considered in this work.

3.3. *The flow near two end zones*

Because the lengthscale in the core flow is R_i, the stream function is independent of θ when $R_i \gg d$ (or $A \ll 1$). However, the lengthscale in the two end zones is d, so stream functions are dependent on both θ and r in these zones. Redefine θ in dimensionless form as follows:

in the entry end: $$\hat{\theta} = \frac{\theta}{A}, \tag{33}$$

in the exit end: $$\hat{\theta} = \frac{\theta - \pi}{A}. \tag{34}$$

The above definition not only readjusts the lengthscale of the flow field, but also assigns $\hat{\theta} = 0$ to the two free surfaces. That is, in the case of $A \to 0$, $\hat{\theta}$ varies from 0 to ∞ as fluid flows from the free surface in the entry end to the core zone; and $\hat{\theta}$ varies from 0 to $-\infty$ as fluid flows from the free surface in the exit end to the core zone.

It is seen from (33) and (34) that $\partial(\,)/\partial\hat{\theta}$ is the same for both the entry and exit end zones, so the governing equations for the two end zones bear the same form. Substituting (33) and (34) into (15) yields

$$\begin{aligned}
&Re\frac{\partial\psi^*}{\partial\hat{\theta}}\left[(A\hat{r}+1)^3\frac{\partial^3\psi^*}{\partial\hat{r}^3} + A(A\hat{r}+1)^2\frac{\partial^2\psi^*}{\partial\hat{r}^2} - A^2(A\hat{r}+1)\frac{\partial\psi^*}{\partial\hat{r}} + (A\hat{r}+1)\frac{\partial^3\psi^*}{\partial\hat{\theta}^2\,\partial\hat{r}} - 2A\frac{\partial^2\psi^*}{\partial\hat{\theta}^2}\right] \\
&\quad - Re\frac{\partial\psi^*}{\partial\hat{r}}\left[(A\hat{r}+1)^3\frac{\partial^3\psi^*}{\partial\hat{r}^2\,\partial\hat{\theta}} + A(A\hat{r}+1)^2\frac{\partial^3\psi^*}{\partial\hat{r}\,\partial\hat{\theta}^2} + (A\hat{r}+1)\frac{\partial^3\psi^*}{\partial\hat{\theta}^3}\right] \\
&= (A\hat{r}+1)^4\frac{\partial^4\psi^*}{\partial\hat{r}^4} + 2A(A\hat{r}+1)^3\frac{\partial^3\psi^*}{\partial\hat{r}^3} - A^2(A\hat{r}+1)\frac{\partial^2\psi^*}{\partial\hat{r}^2} \\
&\quad + A^3(A\hat{r}+1)\frac{\partial\psi^*}{\partial\hat{r}} + 4A^2\frac{\partial^2\psi^*}{\partial\hat{\theta}^2} - 2A(A\hat{r}+1)\frac{\partial^3\psi^*}{\partial\hat{\theta}^2\,\partial\hat{r}} + 2(A\hat{r}+1)^2\frac{\partial^4\psi^*}{\partial\hat{\theta}^2\,\partial\hat{r}^2} + \frac{\partial^4\psi^*}{\partial\hat{\theta}^4}.
\end{aligned} \tag{35}$$

As in the core region, the solution is obtained by the power-series expansion in the small parameter A in the form of

$$\psi^*_{\text{end}} = \psi^*_e = \psi_0 + A\psi_1 + A^2\psi_2 + \ldots. \tag{36}$$

Substituting (36) into (35) and equating terms of like order in A yields

(i) $O(A^0)$:

$$Re\left\{\frac{\partial\psi_0}{\partial\hat{\theta}}\left(\frac{\partial^3\psi_0}{\partial\hat{r}^3} + \frac{\partial^3\psi_0}{\partial\hat{r}\,\partial\hat{\theta}^2}\right) - \frac{\partial\psi_0}{\partial\hat{r}}\left(\frac{\partial^3\psi_0}{\partial\hat{\theta}\,\partial\hat{r}^2} + \frac{\partial^3\psi_0}{\partial\hat{\theta}^3}\right)\right\} = \frac{\partial^4\psi_0}{\partial\hat{r}^4} + 2\frac{\partial^4\psi_0}{\partial\hat{r}^2\,\partial\hat{\theta}^2} + \frac{\partial^4\psi_0}{\partial\hat{\theta}^4}. \tag{37}$$

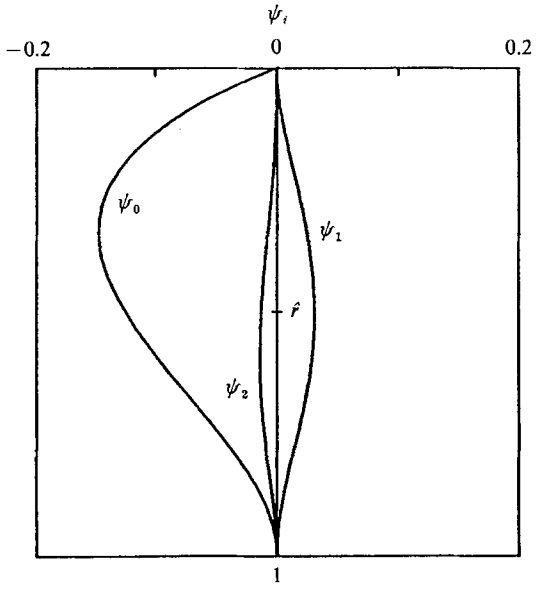

FIGURE 9. Stream functions, ψ_t, in the core zone.

Similarly, substituting (33), (34) and (36) into (16)–(18) yields the zero-order boundary conditions in the form

$$\hat{r} = 0: \qquad \psi_0 = 0, \quad \frac{\partial \psi_0}{\partial \hat{r}} = -1; \tag{38}$$

$$\hat{r} = 1: \qquad \psi_0 = 0, \quad \frac{\partial \psi_0}{\partial \hat{r}} = 0; \tag{39}$$

$$\hat{\theta} = 0: \qquad \psi_0 = 0, \quad \frac{\partial^2 \psi_0}{\partial \hat{\theta}^2} = 0; \tag{40}$$

with the matching conditions given by

$$\lim_{\hat{\theta} \to \pm\infty} \psi_0 \to \psi_{\text{core}} \quad \text{or} \quad \lim_{\hat{\theta} \to \pm\infty} \psi_0 \to -\hat{r}(\hat{r}-1)^2. \tag{41}$$

(ii) $O(A^1)$:

$$\begin{aligned} Re \frac{\partial \psi_0}{\partial \hat{\theta}} \left(3\hat{r} \frac{\partial^3 \psi_0}{\partial \hat{r}^3} + \frac{\partial^2 \psi_0}{\partial \hat{r}^2} + \hat{r} \frac{\partial^3 \psi_0}{\partial \hat{\theta}^2 \partial \hat{r}} - 2 \frac{\partial^2 \psi_0}{\partial \hat{\theta}^2} \right) - Re \frac{\partial \psi_0}{\partial \hat{r}} \left(3\hat{r} \frac{\partial^3 \psi_0}{\partial \hat{r}^2 \partial \hat{\theta}} + \frac{\partial^2 \psi_0}{\partial \hat{r} \partial \hat{\theta}} + \hat{r} \frac{\partial^3 \psi_0}{\partial \hat{\theta}^3} \right) \\ - \left(4\hat{r} \frac{\partial^4 \psi_0}{\partial \hat{r}^4} + 4\hat{r} \frac{\partial^4 \psi_0}{\partial \hat{\theta}^2 \partial \hat{r}^2} + 2 \frac{\partial^3 \psi_0}{\partial \hat{r}^3} - 2 \frac{\partial^3 \psi_0}{\partial \hat{\theta}^2 \partial \hat{r}} \right) \\ = \left(\frac{\partial^4 \psi_1}{\partial \hat{r}^4} + 2 \frac{\partial^4 \psi_1}{\partial \hat{\theta}^2 \partial \hat{r}^2} + \frac{\partial^4 \psi_1}{\partial \hat{\theta}^4} \right) + Re \left\{ \frac{\partial \psi_0}{\partial \hat{r}} \left(\frac{\partial^3 \psi_1}{\partial \hat{r}^2 \partial \hat{\theta}} + \frac{\partial^3 \psi_1}{\partial \hat{\theta}^3} \right) - \frac{\partial \psi_0}{\partial \hat{\theta}} \left(\frac{\partial^3 \psi_1}{\partial \hat{r}^3} + \frac{\partial^3 \psi_1}{\partial \theta^2 \partial \hat{r}} \right) \right. \\ \left. + \left(\frac{\partial^3 \psi_0}{\partial \hat{r}^2 \partial \hat{\theta}} + \frac{\partial^3 \psi_0}{\partial \hat{\theta}^3} \right) \frac{\partial \psi_1}{\partial \hat{r}} - \left(\frac{\partial^3 \psi_0}{\partial \hat{r}^3} + \frac{\partial^3 \psi_0}{\partial \hat{\theta}^2 \partial \hat{r}} \right) \frac{\partial \psi_1}{\partial \hat{\theta}} \right\} \end{aligned} \tag{42}$$

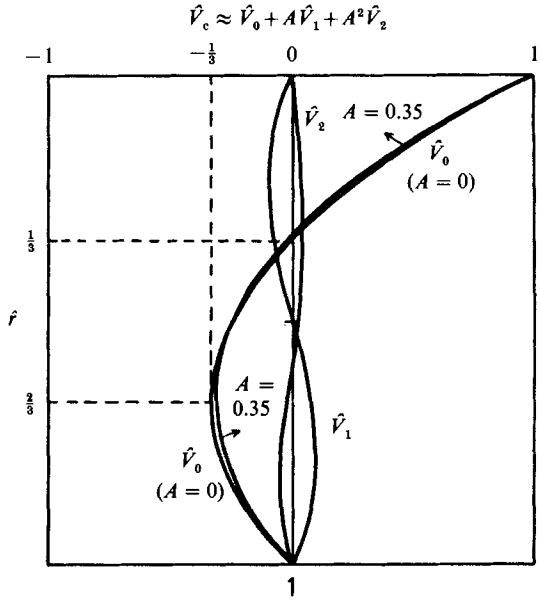

FIGURE 10. Dimensionless velocity distributions in the core zone.

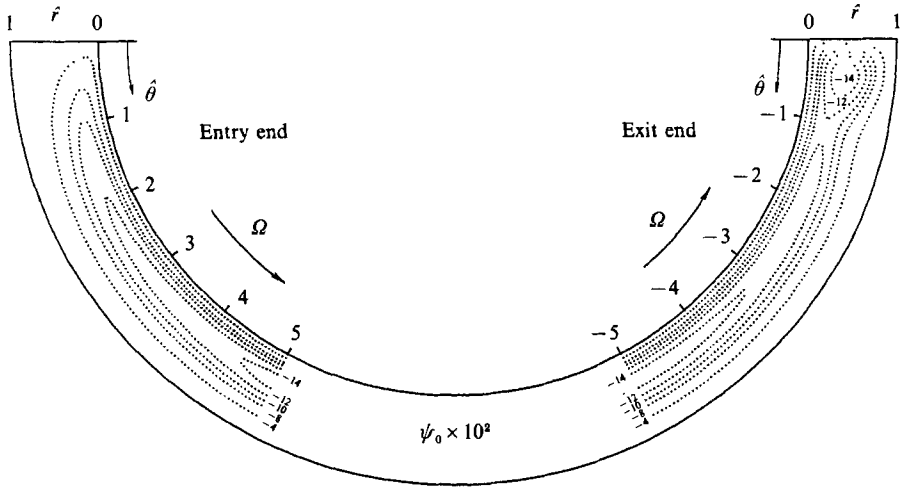

FIGURE 11. Zero-order finite-difference solution, ψ_0, for $Re = 100$.

with boundary conditions:

for $\hat{r} = 0, 1$:
$$\psi_1 = \frac{\partial \psi_1}{\partial \hat{r}} = 0, \tag{43}$$

for $\hat{\theta} = 0$:
$$\psi_1 = \frac{\partial^2 \psi_1}{\partial \hat{\theta}^2} = 0, \tag{44}$$

and matching conditions:
$$\lim_{\hat{\theta} \to \pm\infty} \psi_1 \to \tfrac{1}{2}\hat{r}^2(\hat{r}-1)^2, \tag{45}$$

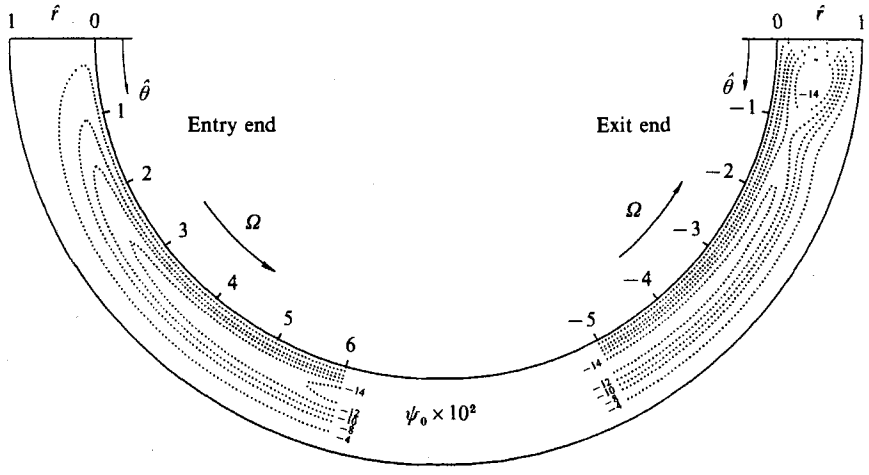

FIGURE 12. Zero-order finite-difference solution, ψ_0, for $Re = 200$.

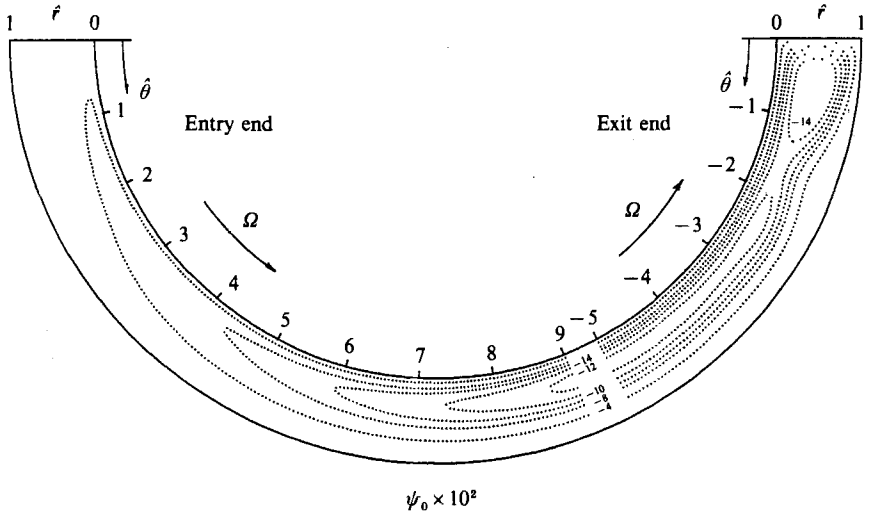

FIGURE 13. Zero-order finite-difference solution, ψ_0, for $Re = 400$.

where the plus signifies the entry end and the minus the exit end. It can be seen that governing equation (42) for ψ_1 contains the curvature effect ($\hat{r}$), but governing equation (37) for ψ_0 does not.

3.4. *Zero- and first-order finite-difference solutions in the two end zones*

The above governing equations together with the boundary and matching conditions for the two end zones are solved by the finite-difference method. Since detailed descriptions of the calculation procedures are given in Chan (1988), only brief remarks are summarized below.

A 13-point finite-difference formula was used for each interior point, and a central-difference approximation for all boundary points. All results presented in this paper were obtained using a uniform 20×20 grid system. Checks were made by comparing

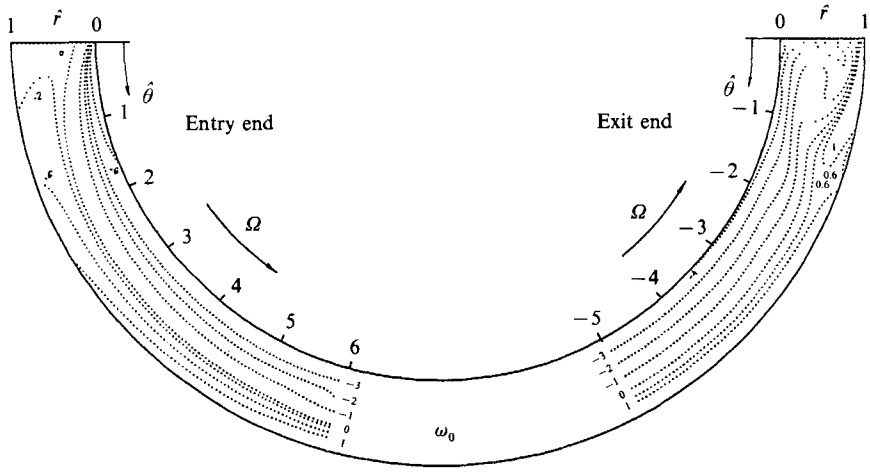

FIGURE 14. Zero-order finite-difference solution, ψ_0, for $Re = 200$.

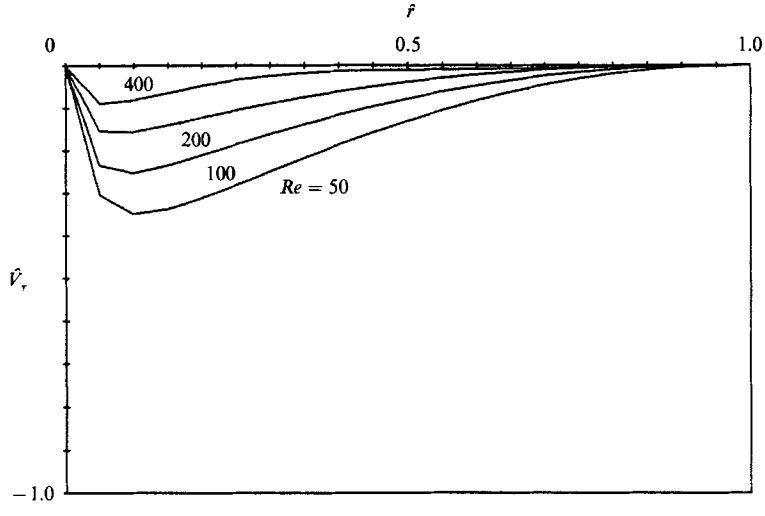

FIGURE 15. Dimensionless velocity distributions along the free surface at the entry end.

the results from a 20×20 grid system with those from a 40×40 grid system, and agreement was very satisfactory.

Point iteration in conjunction with the successive relaxation procedure was employed in the calculation. The convergence criterion at each point is

$$\mathrm{Max}\left(\left|\frac{\psi_{j,k}^{n+1} - \psi_{j,k}^{n}}{\psi_{j,k}^{n}}\right|\right) \leqslant 5 \times 10^{-4},$$

where superscript n denotes to the iteration number, and subscript (j, k) denotes to the mesh location in the $(\hat{r}, \hat{\theta})$-domain. The above finite-difference scheme has been used by Bye (1966), and more recently by Schreiber & Keller (1983). In the present study, matching conditions for $\hat{\theta} \to \pm\infty$ were satisfied at $\hat{\theta}_{\max} = 5$–9. The CPU time on a CDC CYBER 180/840A was approximately 400 to 2000 s, depending on the Re and the relaxation parameter.

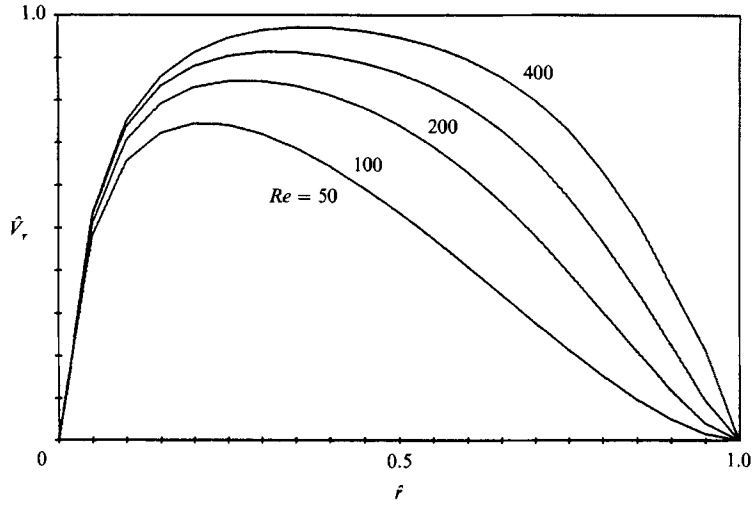

FIGURE 16. Dimensionless velocity distributions along the free surface at the exit end.

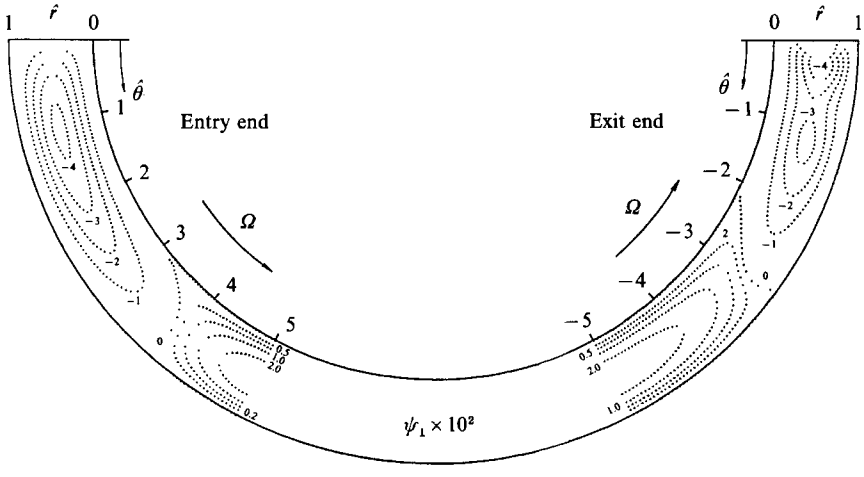

FIGURE 17. First-order finite-difference solution, ψ_1, for $Re = 50$.

3.5. *Results*

3.5.1. *The core flow*

The streamfunction ψ_i for $i = 0, 1, 2$ in the core zone are given in (27)–(29) and presented in figure 9, which shows that values of ψ_i decay rapidly as the order i increases. The velocities $\hat{V}_i$ for $i = 0, 1, 2$ are given in (30)–(32) and presented in figure 10. Figure 10 also shows the composite solution $\hat{V}$ resulting from the leading three terms for $A = 0.35$. It is seen that two curves for $\hat{V}$ and $\hat{V}_0$ agree very well: that is, the zero-order solution is dominant. The velocity profile of $\hat{V}_0$ in figure 10 shows a zero-crossing point at $\hat{r}_c = \frac{1}{3}$: that is, the inner fluid layer ($\hat{r} < \hat{r}_c$) moves in the same direction as the roller, and the outer fluid ($\hat{r} > \hat{r}_c$) moves in the reverse direction. The maximum reversed velocity is $\hat{V}_{max} = -\frac{1}{3}$ at $\hat{r} = \frac{2}{3}$. Note that $\hat{V}_0$ in (30) is the same as that obtained by Brewster *et al.* (1959).

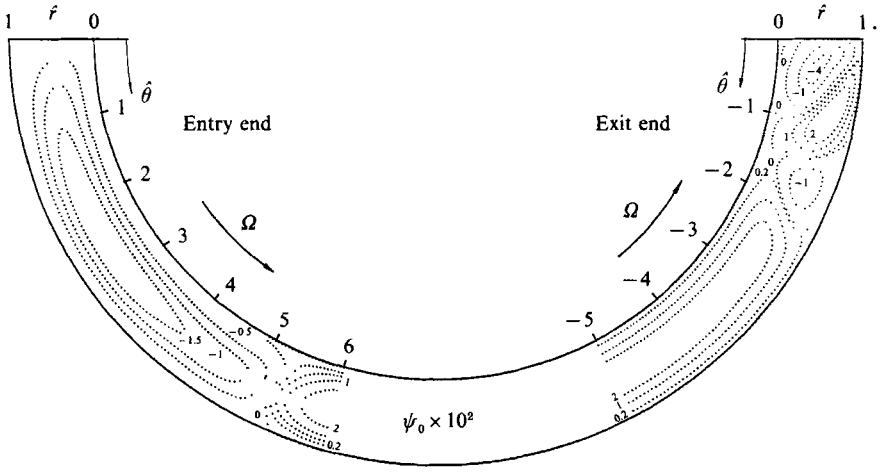

FIGURE 18. First-order finite-difference solution, ψ_1, for $Re = 200$.

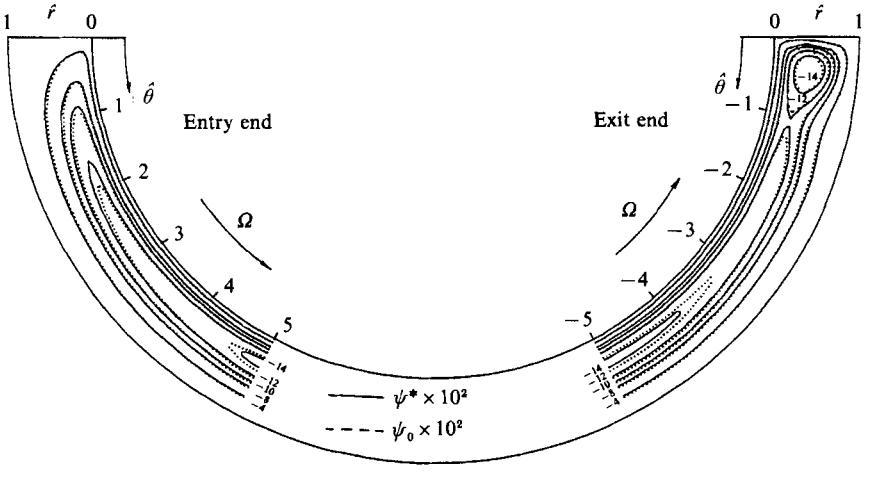

FIGURE 19. Streamlines for $A = 0.2$ and $Re = 100$: ——, composite solution; ----, zero-order solution.

3.5.2. *Finite-difference solutions in the two end zones*

The zero-order streamlines, ψ_0, obtained by the finite-difference method are shown in figures 11, 12, and 13 for $Re = 100$, 200 and 400, respectively. These figures also show that fluid makes a smooth 180° turn at the entry end, but makes a 180° turn with a vortex cell and necking at the exit end. As Re increases, streamlines in the inner layer become closer together, but in the outer layer become farther apart. All these results are in good agreement with those obtained by the flow visualization results.

The zero-order vorticity lines, ω_0, for $Re = 200$ are shown in figure 14. It is seen that the vorticity at the exit end is much stronger than at the entry end, and vortex lines are almost parallel elsewhere.

The dimensionless velocity distributions, $\hat{V}_r$, along the two free surfaces are shown

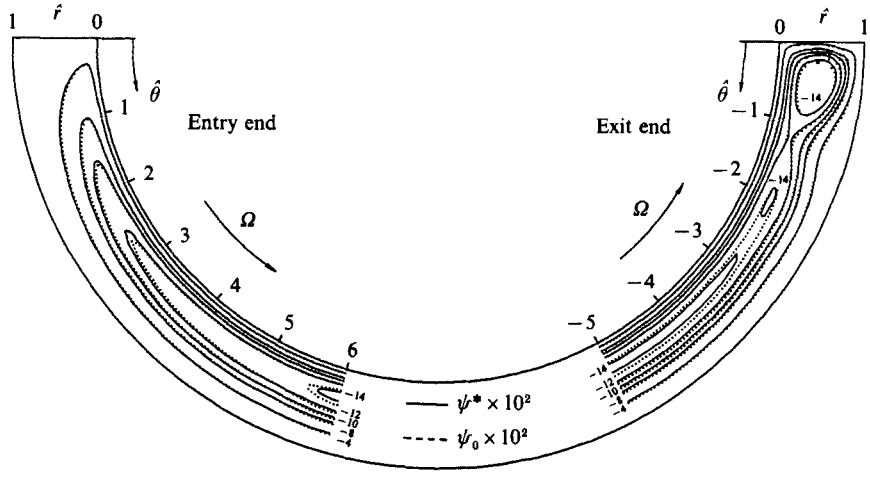

FIGURE 20. Streamlines for $A = 0.2$ and $Re = 200$: ——, composite solution; ----, zero-order solution.

in figures 15 and 16. Figure 15 shows that, as Re increases, $\hat{V}_r$ decreases and the location of the peak value moves closer to the inner cylinder in the entry end. However, at the exit end shown in figure 16, as Re increases $\hat{V}_r$ increases and the location of the peak value moves closer to the outer cylinder.

The first-order streamlines, ψ_1, obtained by the finite-difference method are shown in figures 17 and 18 for $Re = 50$ and 200, respectively. As mentioned above, the governing equations for ψ_1 contain the curvature ($\hat{r}$) effect. It is seen from figures 17 and 18 that there are several vortex cells with dividing lines between them. As Re increases, the vortex cell becomes larger and the dividing line moves towards the core zone in the entry end. But as Re increases, the number of vortex cells increases and the dividing line moves closer to the free surface in the exit end.

From (22), the composite solution resulting from the leading two terms is

$$\psi^* = \psi_0 + A\psi_1 \tag{46}$$

The streamlines of the composite solution for $A = 0.2$ and $Re = 100$ and 200 are shown in figures 19 and 20, respectively. In the figures, solid lines represent the streamlines obtained from (46) and dashed lines represent the zero-order solution. It is seen that ψ_0 compares very well with ψ^*. The only noticeable modification of ψ_1 appears at $Re = 200$, where there is an even smaller cell below the necking place at the exit end. This is also in good agreement with the visualization pattern shown in figure 3 (d).

The velocity distributions at various θ-sections at the entry and exit ends are shown in figures 21 (*a*) and 21 (*b*), respectively. The solid lines are the composite solution for $A = 0.3$; and dashed lines are the zero-order solution $\hat{V}_0$. The figures, apart from the small modifications of the first-order solution at the exit end, compare very well. That is, for small value of A, the zero-order solution is dominant and the curvature effect is negligible.

3.5.3. *Validation range of A*

The composite solution given in (46) has truncation error of $O(A^2)$. Since matching conditions require the existence of the core flow, it follows from (33) or (34) that the

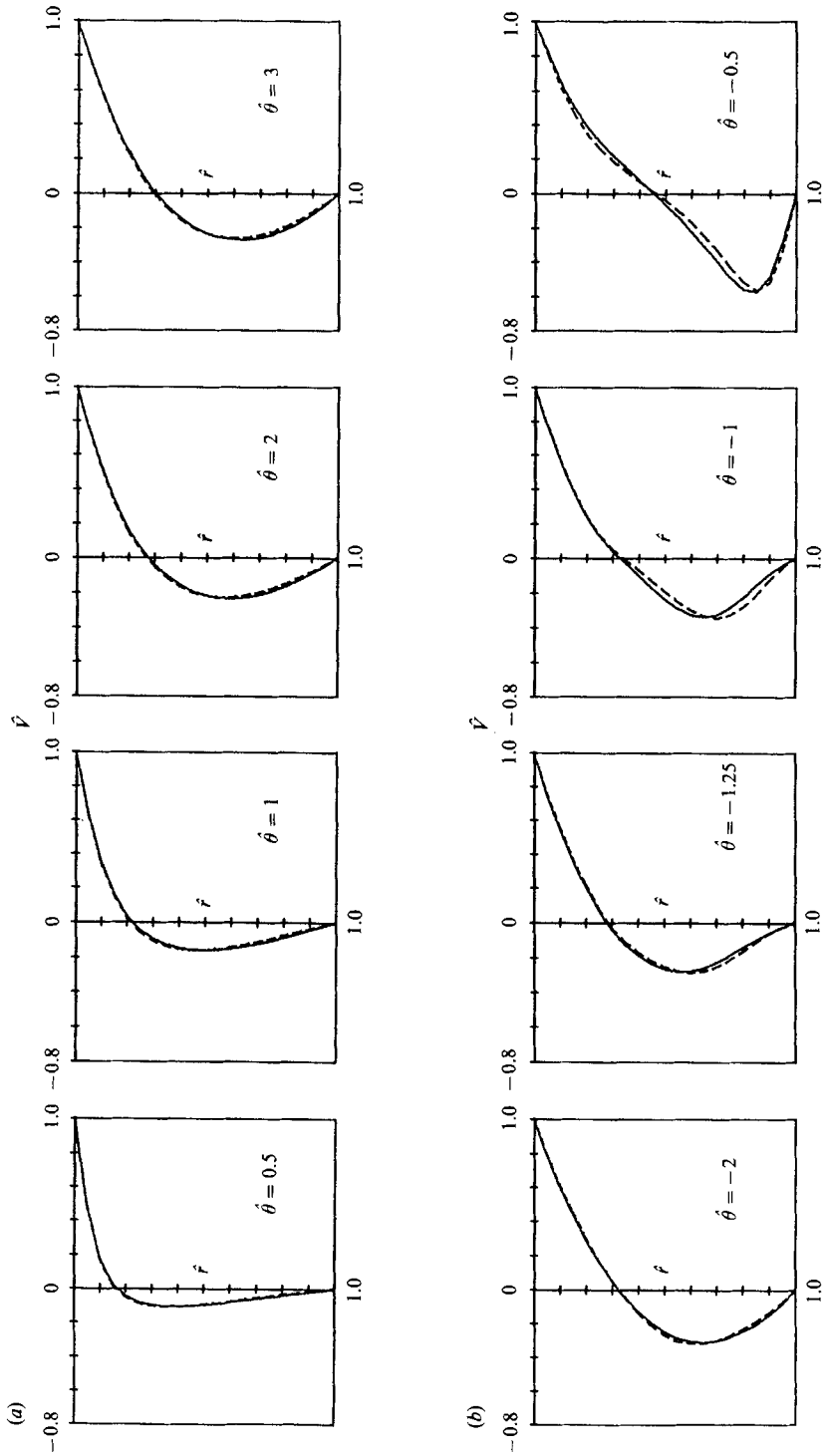

FIGURE 21. Dimensionless velocity distributions at various θ-sections: (*a*) at the entry end, (*b*) at the exit end; ——, composite solution; ----, zero-order solution.

range of A for which the asymptotic solution is valid can be obtained according to the following formula:

$$A_u = \frac{\pi}{L_{en}+L_{ex}+L_{core}}, \tag{47}$$

where A_u is the upper limit of the aspect ratio A, L_{en} the convergence length of θ in the entry end, L_{ex} the convergence length of θ in the entry end, L_{ex} the convergence length of θ in the exit end, and $L_{core} = 0$, the limiting case for which parallel core exists. That is, the evaluation of A_u is based on an estimate of when the flow in the two end regions would just reach each other. Values of L_{en} and L_{ex} can be extracted from the results in figures 11 and 13 as follows:

for $Re = 100$: $\quad L_{en} \approx 5, \quad L_{ex} \approx 5;$

for $Re = 400$: $\quad L_{en} \approx 9, \quad L_{ex} \approx 5.$

It follows from (47) that $A_u = 0.31$ for $Re \leqslant 100$, $A_u = 0.22$ for $Re \leqslant 400$: that is, A_u decreases as Re increases.

4. Comparison of experimental and theoretical results

As described in the previous sections the streamlines obtained by asymptotic expansions in conjunction with the finite-difference method compare fairly well with the visualization patterns for the laminar regime. These include the parallel flow in the core zone, the presence of the vortices of the exit end and their absence from the entry end. Quantitative comparisons are also made by examining the velocity distributions at various radial sections, as is shown in figure 22, where the solid lines represent the composite solutions and the points represent the measurements for $Re = 215$ and $A = 0.137$. It is seen that comparisons of the velocity profiles, such as the zero-crossing points and maximum reversed velocity between the experimental and theoretical results agree very well. This further supports the notion that the curvature effect is negligible for small values of aspect ratio A.

5. Summary

The results of an experimental and theoretical study of the flow in a half-filled annulus between horizontal concentric cylinders with the inner one rotating and the outer one at rest have been presented. A laser-Doppler velocimeter was used to obtain the velocity distributions both in the laminar and turbulent regimes for aspect ratio $A = 0.137$. Dye visualizations were also used to observe the flow patterns. Theoretical results from asymptotic expansions in the limit of small aspect ratio A were obtained. Various features of the flow predicted in the analyses, in particular the presence of vortices in the exit end region and their absence from the entry end region, are confirmed by the experimental results.

The following conclusions are drawn from this study:

(*a*) The thickness of the bottom fluid layer adjacent to the inner cylinder is about half of that adjacent to the inner one in the laminar regime. The inner (outer) fluid layer is thinner (thicker) in the turbulent regime than that in the laminar regime.

(*b*) Flow characteristics, such as zero-crossing point, and maximum reversed velocity and its radial position vary more significantly in the two end zones than in the core zone. Turbulent velocity near the inner cylinder is larger than that near the outer cylinder.

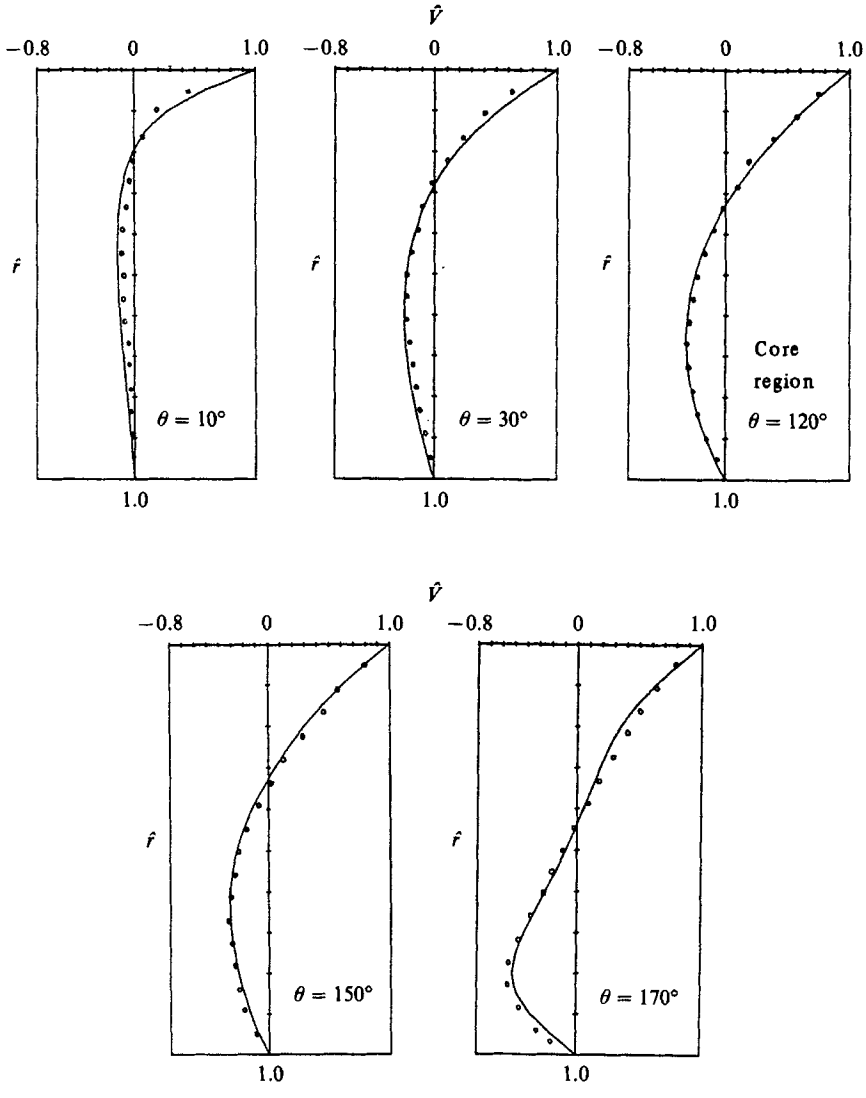

FIGURE 22. Comparison between composite solution (——) and experimental data (○) for $Re = 215$ and $A = 0.137$.

(*c*) For small aspect ratio A, the zero-order solution is dominant throughout the entire flow field. The first-order solution or curvature effect makes a small modification to the composite solution only in the exit end zone at high Re. Vorticity is strongest of the exit end. The upper limit for which asymptotic solutions are valid decreases with increasing Re; for example, $A_u = 0.31$ for $Re \leqslant 200$ and $A_u = 0.22$ for $Re \leqslant 400$.

(*d*) Various flow regimes are identified from the measurements of the local moment coefficient and visualization results. These are:

$Ta < 92$:	laminar regime	
$92 < Ta < 150$:	unstable laminar transition	transition
$150 < Ta < 500$:	turbulent growth	
$Ta > 500$:	fully turbulent.	

There should be further investigation of the non-vanishing normal stress boundary conditions to determine the shape of the interfaces (without the assumption of flat free-surfaces). Because the flow field in the bottom core zone is parallel and independent of the Reynolds number, work is being done to obtain the zero-order solutions in the two end regions by the linearized method in the limit as $Re \to 0$.

Partial support of this work by China Steel Corporation in Taiwan through Grant TRC-75-06 is greatly acknowledged.

REFERENCES

BREWSTER, D. B., GROSBERG, P. & NISSAN, A. H. 1959 The stability of viscous flow between horizontal concentric cylinders. *Proc. R. Soc. Lond.* A **251**, 76–91.

BYE, J. A. T. 1966 Numerical solution of steady-state vorticity equation in rectangular basins. *J. Fluid Mech.* **26**, 577–598.

CHAN, T. M. 1988 Theoretical investigation of laminar flow in half-filled, horizontal, concentric, cylinders with inner one rotating and outer one at rest. M.S. Thesis, Dept. of Mech. Engng, National Sun Yat-Sen University, Taiwan.

CHEN, K. S. & CHAN, T. M. 1988 Local-nonsimilar solutions of laminar flow in half-filled horizontal concentric cylinders with inner one rotating and outer one at rest. *In 3rd Intl Symp. on Transport Phenomena in Thermal Control, Taipei, Taiwan*, pp. 679–692.

CHEN, K. S., YANG, S. Z. & HUMPHREY, J. A. C. 1988 Experimental investigation of flow in half-filled horizontal concentric cylinders with inner one rotating and outer one at rest. In *3rd Intl Symp. on Transport Phenomena in Thermal Control, Taipei, Taiwan*, pp. 693–705.

COLES, D. 1965 Transition in circular Couette flow. *J. Fluid Mech.* **21**, 385–425.

DAVEY, A. 1962 The growth of Taylor vortices in flow between rotating cylinders. *J. Fluid Mech.* **14**, 336–368.

DUTY, R. L. & REID, W. H. 1964 On stability of viscous flow between rotating cylinder. *J. Fluid Mech.* **20**, 81–94.

KOMODA, A. Y. 1983 An outline of new electro-galvanizing line (KMRCEL). *Kawasaki Steel Tech. Rep.* 8, pp. 17–27.

MEKSYN, D. 1946 Stability of viscous flow between rotating cylinders. *Proc. R. Soc. Lond.* A **187**, 115–128.

NABATAME, M. 1984 An outline of Fukuyama no. 3 electrolytic galvanizing line. *Nippon Kokan Tech. Rep. (Overseas)* 40, pp. 9–16.

SCHREIBER, R. & KELLER, H. B. 1983 Driven cavity flow by efficient numerical techniques. *J. Comput. Phys.* **49**, 310–333.

STEINMAN, H. 1956 The stability of viscous flow between rotating cylinders. *Q. Appl. Maths* **14**, 27–33.

STUART, J. T. 1958 On nonlinear mechanics of hydrodynamic stability. *J. Fluid Mech.* **4**, 1–21.

TAYLOR, G. I. 1923 Stability of a viscous liquid contained between two rotating cylinders. *Phil. Trans. R. Soc. Lond.* A **223**, 289–343.

TAYLOR, G. I. 1936 Fluid friction between rotating cylinders. I. Torque measurements. *Proc. R. Soc. Lond.* A **57**, 546–564.

WHITE, F. M. 1978 *Viscous Fluid Flow*. McGraw Hill.